A Novel Signal Processing Technique for Ku-Band Automobile FMCW Fully Polarimetric SAR System Using Triangular LFM

Dae-Hwan Jung, Do-Hoon Kim, Muhammad Tayyab Azim, Junhyeong Park, *Member, IEEE*, and Seong-Ook Park, *Senior Member, IEEE*

***Abstract*— This article presents a novel signal technique for Ku-band automobile frequency-modulated continuous-wave fully polarimetric synthetic aperture radar (FMCW PolSAR) system using triangular linear frequency modulation (LFM). Our proposed system shows the first utilizations of triangular LFM for an FMCW PolSAR. The proposed signal processing algorithm is based on the range Doppler algorithm (RDA). We developed an FMCW PolSAR system that transmits triangular LFM signals, which are used less frequently than sawtooth LFM in an SAR sensor. Using a theoretical background, we describe its configuration and how it works. We propose the novel processing solution, which forms two kinds of single-polarization images from a raw data set and is suitable for our system. We obtained all four kinds of single-polarization images from two raw data sets while using the triangular LFM. In comparison, when using sawtooth LFM, we obtained the four images from four raw data sets by repeating the RDA four times. The proposed method simplifies the FMCW PolSAR system configuration and the processing algorithm. We collected FMCW PolSAR raw data from an experimentally equipped automobile while maintaining a constant speed on a highway. The proposed algorithm and system were validated by processing a high-resolution FMCW PolSAR image.**

***Index Terms*— Automobile synthetic aperture radar (SAR), frequency modulated continuous wave (FMCW) radar, fully polarimetric SAR (PolSAR), linear frequency modulation (LFM), range Doppler algorithm (RDA), SAR, triangular waveform.**

List of Acronyms and Abbreviations

ADC	Analog-to-Digital Converter.
CR	Corner Reflector.
DDS	Direct Digital Synthesizer.
FFT	Fast Fourier Transform.
FMCW	Frequency-Modulated Continuous-Wave.
HH	Horizontal to Horizontal.
HH-pol	HH Polarimetric.
H-pol	Horizontally Polarized.
HV	Horizontal to Vertical.
HV-pol	HV Polarimetric.
IFFT	Inverse Fast Fourier Transform.
IQ	In-phase and Quadrature.
LFM	Linear Frequency Modulation.
MTI	Moving Target Indicator.
PRF	Pulse-Repetition-Frequency.
PRI	Pulse-Repetition-Interval.
PolSAR	Polarimetric Synthetic Aperture Radar.
PSLR	Peak Sidelobe Ratio.
RCM	Range Cell Migration.
RCMC	Range Cell Migration Correction.
RDA	Range Doppler Algorithm.
RF	Radio Frequency.
RX	Receiver.
TX	Transmitter.
VH	Vertical to Horizontal.
VH-pol	VH Polarimetric.
V-pol	Vertically Polarized.
VV	Vertical to Vertical.
VV-pol	VV Polarimetric.

Manuscript received March 12, 2020; accepted July 12, 2020. Date of publication July 24, 2020; date of current version December 7, 2020. This work was supported by the Institute for Information & Communications Technology Planning & Evaluation (IITP) Grant funded by the Korea Government (MSIT) (Key Technologies Development for Next Generation Satellites) under Grant 2018-0-01658. The Associate Editor coordinating the review process was Dr. Dong Wang. *(Corresponding author: Dae-Hwan Jung.)*

The authors are with the School of Electrical Engineering, Korea Advanced Institute of Science and Technology, Daejeon 34141, South Korea (e-mail: daeman88@kaist.ac.kr; dohoonh@kaist.ac.kr; tayyabazim@kaist.ac.kr; bdsfh0820@kaist.ac.kr; soparky@kaist.ac.kr).

Digital Object Identifier 10.1109/TIM.2020.3011601

I. Introduction

FREQUENCY-MODULATED continuous-wave (FMCW) radar has recently received a great deal of attention because it offers advantages including low constant transmission power, small size, and low manufacturing cost [1]–[3]. The number of applications for FMCW radar is also rapidly expanding in various research areas. One of these areas is synthetic aperture radar (SAR) [4]–[6]. In earlier years, the number of SAR sensors based on a type of pulsed radar was larger than that of FMCW SAR sensors. But recently, with advances in signal generation hardware, FMCW SAR sensors have become attractive alternatives, giving rise to high-resolution FMCW radar systems. In addition, the benefits of FMCW radar have led to particular interest in SAR polarimetry, which provides an effective means of deriving qualitative and quantitative physical information from a detection area (e.g., land, ocean, and urban areas) [7]–[9]. FMCW polarimetric SAR (PolSAR) was first introduced in [10].

Yamaguchi and Moriyama [10] detected objects buried in a snowpack with FMCW PolSAR. However, their produced images differed significantly from the general terrain images of PolSAR. In other words, their results were unable to achieve the main objective of PolSAR tomography.

In FMCW radar, a linear frequency modulation (LFM) signal, such as a sawtooth waveform or a triangular waveform, is typically utilized to simultaneously extract both target range and velocity information from a received signal. Useful waveforms are constrained by the type of applications. In the FMCW SAR field, to reduce azimuth ambiguities, a sawtooth waveform is usually employed. The waveform provides an effective way of producing a pulse-repetition-frequency (PRF) that is higher than a triangular waveform [4], [5], [11]. Nevertheless, much excellent work has been accomplished on FMCW SAR by exploiting other waveforms. Wang *et al.* [12] described a new approach based on waveform diversity to resolve range and azimuth ambiguities in FMCW unmanned airborne vehicle SAR systems. Meta and Hoogeboom [13] addressed the effect of a moving target in an SAR image produced by an FMCW SAR system with a triangular waveform as the LFM method; this can be utilized to assist moving target indicator (MTI) capabilities.

However, in the FMCW PolSAR field, only the sawtooth waveform has been employed.

FMCW radar has been gaining popularity as a substitute for pulsed radar, and it is becoming increasingly important to focus FMCW PolSAR research on FMCW radar features, such as triangular LFM and range fast Fourier transform (FFT) for range compression with the range-Doppler algorithm (RDA).

In this article, we propose a new signal processing algorithm for FMCW PolSAR systems which employs the triangular waveform as an LFM method for detecting numerous targets on the ground. Using our proposed algorithm, an FMCW PolSAR system with triangular LFM was determined to be simpler than one using sawtooth LFM.

In a system radiating sawtooth waveforms, it is usually essential to acquire digital data from a square wave, which is created for synchronization. The data are needed to separate the vertical to vertical (VV), horizontal to vertical (HV), vertical to horizontal (VH), and horizontal to horizontal (HH) raw data coming into each receiver (RX). Using triangular LFM, our method is capable of separating the raw data without the square wave digital data. This makes it unnecessary to include an analog-to-digital converter (ADC) for the square wave in the FMCW PolSAR system using triangular LFM, which simplifies the FMCW PolSAR system configuration. By applying range FFT as the range compression RDA, the positional information of targets appears to be symmetrically overlapped in the frequency domain because of the upslope and downslope parts of the triangular waveform.

We constructed two data sets by exploiting this feature of the triangular waveform: 1) a data set with symmetrical overlap between a VV and an HV image and 2) a data set with symmetrical overlap between a VH and an HH image. In a system using sawtooth LFM, one data set is generally required for each polarization image. Four data sets are needed for a fully PolSAR image in the case of the sawtooth LFM. We showed that the triangular waveform leads to simplification of the algorithm for FMCW PolSAR.

Here, we describe a remarkable way of separating the two kinds of single-polarization images overlapped in the same scene. To validate our algorithm, we not only designed a Ku-band FMCW fully PolSAR system but also performed a field test with the system on a moving automobile platform. Utilizing the automobile platform for system verification also demonstrated benefits of low cost and easy modification [14]–[16]. A defined FMCW PolSAR image was produced by our proposed algorithm using raw data acquired in the field test.

The remainder of this article is organized as follows. Section II provides the FMCW SAR signal model based on triangular LFM waveform. Section III introduces our FMCW PolSAR system and a new signal processing algorithm for FMCW PolSAR using triangular LFM. Section IV discusses the field test with our system mounted on an automobile. In addition, a high-resolution FMCW PolSAR image is presented to validate our proposed algorithm and the developed system. Finally, conclusions for this article are provided in Section V.

II. FMCW SAR Signal Model Based on Triangular LFM Waveform

A. FMCW Radar Using Triangular LFM Waveform

We present a basic theory of FMCW radar based on sawtooth and triangular LFMs. The signal transmitted from an FMCW radar can be expressed as [17], [18]

$$s_{\mathrm{TX}}(t) = \exp\left\{ j2\pi \left(f_{\mathrm{c}}t + \frac{1}{2}\frac{B_{\mathrm{swp}}}{T_{\mathrm{swp}}}t^2 \right) \right\} \tag{1}$$

where f_{c} is the carrier frequency, B_{swp} is the LFM sweep bandwidth of the transmitted baseband signal, T_{swp} is the pulse repetition interval (PRI), and t is the time variable within PRI. B_{swp} and T_{swp} are constants since we assume that LFM is applied. Equation (1) is valid for the upslope sawtooth LFM and the upslope parts of the triangular LFM, as shown in Fig. 1(a) and (b). We assume that there is a single target on the ground. After reflecting off the stationary target, the received radar signal is derived as

$$s_{\mathrm{RX}}(t) = \exp\left\{ j2\pi \left(f_{\mathrm{c}}(t-\tau) + \frac{1}{2}\frac{B_{\mathrm{swp}}}{T_{\mathrm{swp}}}(t-\tau)^2 \right) \right\} \tag{2}$$

where τ is the time delay generated by the target. After mixing the transmitted and received signals with a mixer, the intermediate frequency is described as

$$s_{\mathrm{IF,up}}(t) = \exp\left\{ j2\pi \left(-f_{\mathrm{c}}\tau - \frac{B_{\mathrm{swp}}}{T_{\mathrm{swp}}}\tau t + \frac{1}{2}\frac{B_{\mathrm{swp}}}{T_{\mathrm{swp}}}\tau^2 \right) \right\}. \tag{3}$$

The second phase term in (3) is proportional to the time delay. This term is called the beat frequency. We exploit the beat frequency to extract the target range information, which can be determined by applying an FFT. For the downslope part of the triangular LFM, the intermediate frequency, which is slightly different than (3), is derived as

$$s_{\mathrm{IF,down}}(t) = \exp\left\{ j2\pi \left(-f_{\mathrm{c}}\tau + \frac{B_{\mathrm{swp}}}{T_{\mathrm{swp}}}\tau t - \frac{1}{2}\frac{B_{\mathrm{swp}}}{T_{\mathrm{swp}}}\tau^2 \right) \right\}. \tag{4}$$

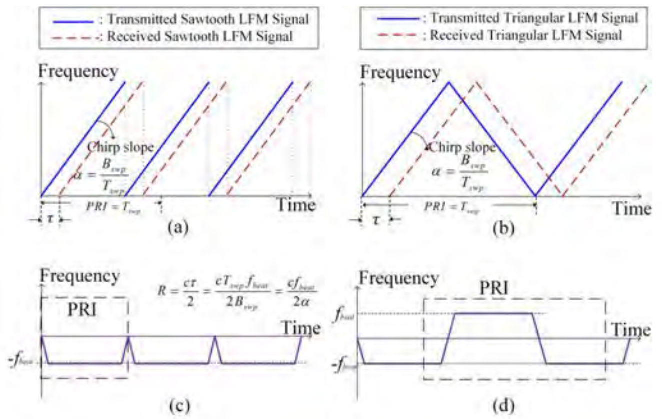

Fig. 1. Behavior of signals at different stages to a generated beat frequency, for sawtooth and triangular LFM transmission signals from a numerical simulation and an experiment. (a) Transmitted and received sawtooth LFM signals from the numerical simulation. (b) Transmitted and received triangular LFM signals from the numerical simulation. (c) Beat frequency in the negative region after deramping of transmitted and received signals in the case of sawtooth LFM from the numerical simulation. (d) Beat frequency in both the negative and the positive regions after deramping of transmitted and received signals in the case of triangular LFM from the numerical simulation.

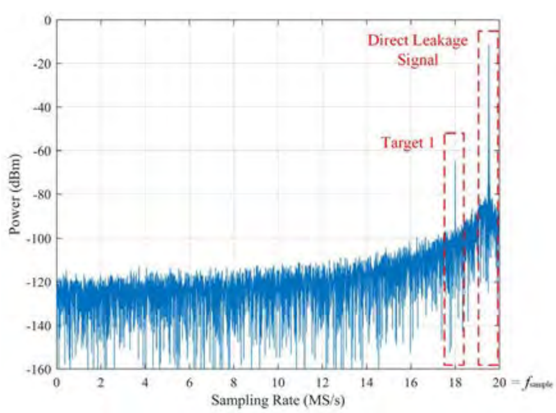

Fig. 2. Beat frequency in the frequency domain in the case of sawtooth LFM from the simulation in MATLAB.

From the second phase term in (3) and (4), we can confirm that the beat frequency appears in the negative frequency region for the upslope sawtooth LFM and the upslope parts of the triangular LFM, whereas the beat frequency appears in the positive region for the downslope parts of the triangular LFM.

Figs. 1–3 show how the beat frequency is generated by the sawtooth and triangular LFM waveforms from a numerical simulation. Figs. 1–3 are from the numerical simulation in MATLAB. We conducted the simulation with the parameters described in Table I to briefly show how the beat frequency appears in the frequency domain as presented in Figs. 2 and 3. The FMCW radar radiates signals in the form of each LFM and receives the signals reflected back from a target after a certain time delay. For the sawtooth LFM as described in Fig. 1(a), after deramping of the transmitted and received signals, the beat frequency appears in the negative frequency region in the second phase term of (3), as shown in Fig. 1(c).

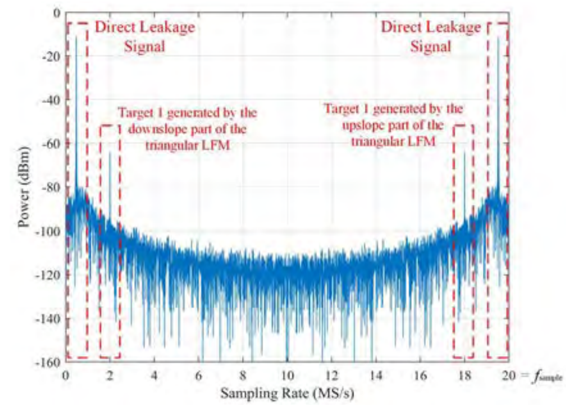

Fig. 3. Beat frequency in the frequency domain in the case of triangular LFM from the simulation in MATLAB.

TABLE I

SPECIFICATIONS OF THE SIMULATION IN MATLAB

Parameters	Specifications
LFM Sweep Bandwidth	500 MHz
PRI	200 μs
LFM Sweep Types	Sawtooth, Triangular LFM
Center Frequency	14.25 GHz
Sampling Rate	20MS/s
Direct Leakage Delay	28.8m
Range to Target 1	120m
Window	Hann

We applied FFT to samples corresponding to PRI to produce samples in the frequency domain. Fig. 2 illustrates the beat frequency in the frequency domain, which appears negative from the sampling frequency.

Since our FMCW PolSAR system utilizes in-phase and quadrature (*IQ*) modulation, it is capable of detecting a target range using a whole sampling frequency, f_{sample}. We marked the range from zero to f_{sample} to draw a continuous beat frequency waveform, as presented in Fig. 2. There are two peaks in Fig. 2: 1) a direct leakage signal directly from the transmitter (TX) to the RX and 2) the beat frequency generated by the target. In the case of the triangular LFM, the beat frequency is generated by alternating the positive and negative frequency region, according to the second phase term in (3) and (4), as shown in Fig. 1(d). Fig. 3 is a result of the beat frequency in the frequency domain after applying FFT to samples within PRI. It has a form where the beat frequency generated by the upslope and the downslope parts of the triangular LFM overlaps symmetrically. In our proposed algorithm as presented in Section III, we exploit the feature of the triangular LFM, which is the symmetrical beat frequency. Using the second phase term in (3) and (4), the detection range to the target can be derived as

$$R = \frac{c\tau}{2} = \frac{cT_{\text{swp}} f_{\text{beat}}}{2B_{\text{swp}}} = \frac{cf_{\text{beat}}}{2\alpha} \tag{5}$$

where α is the frequency sweep rate equal to the ratio between B_{swp} and T_{swp}.

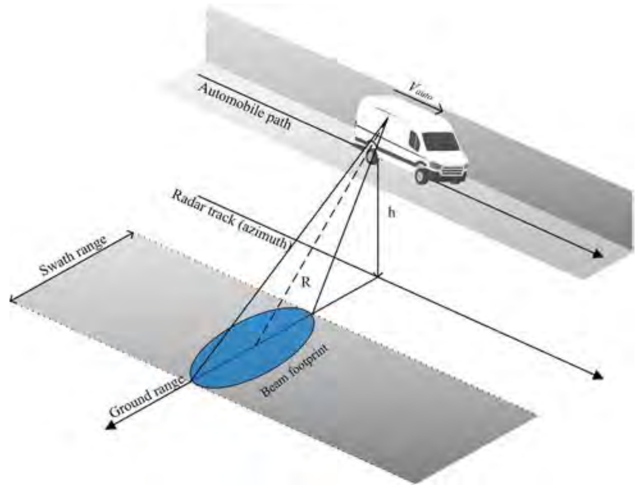

Fig. 4. Automobile FMCW PolSAR geometry in the zero-squint case.

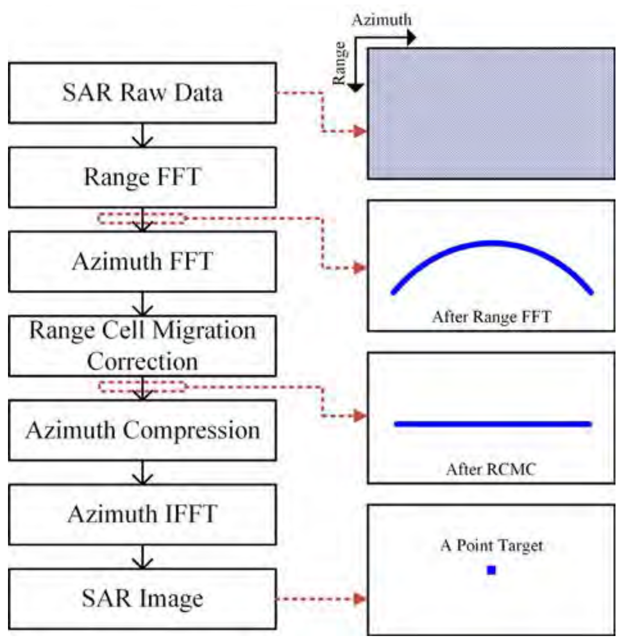

Fig. 5. RDA for FMCW SAR in the zero-squint case.

B. FMCW SAR Signal Model Using Triangular Waveform

Fig. 4 shows the automobile FMCW PolSAR geometry in the zero-squint case. We exploited RDA as a signal processing scheme to form an FMCW SAR image, as detailed in Fig. 5. The raw data collected on the SAR platform consisted of unidentifiable data. In RDA, the first step is to perform range compression in the range direction. In a conventional SAR system based on pulse radar, several steps using a matched filter are usually required for range compression: range FFT, matched filtering, and range inverse FFT (IFFT). For the SAR system based on FMCW radar, range FFT can be used to simply replace the range compression step. This enables the algorithm to be simple, and the elapsed signal processing time for an SAR image is decreased.

From (3)–(5), the data received from the point target after range FFT can be expressed as [19]

$$\begin{aligned} S_{rc}(f_\tau, \eta) &\approx A_0\, w_{\mathrm{a}}(\eta - \eta_{\mathrm{c}}) \\ &\quad \times \{W_{\mathrm{r,up}}[-f_\tau - f_{\mathrm{beat,up}}] + W_{\mathrm{r,down}}[f_\tau - f_{\mathrm{beat,down}}]\} \\ &\quad \times \exp\left\{-j\frac{4\pi f_{\mathrm{c}} R_0}{c}\right\} \exp\{-j\pi K_{\mathrm{a}}\eta^2\} \end{aligned} \tag{6}$$

where A_0 is the magnitude of the point target, which means the backscatter coefficient, η is the azimuth time, which is the time domain in the azimuth direction, W_{r} is the compressed pulse envelope in the range direction, w_{a} is the received signal strength as the function of azimuth time, η_{c} is the beam center-crossing time, which is the difference between the time when the sensor approaches closest to the scene center, R_0 is the range of the closest approach to a target, and K_{a} is the azimuth frequency modulation rate, which is the rate of change of Doppler frequency.

As the next step in RDA, we conducted azimuth FFT to perform range cell migration correction (RCMC) in the range Doppler domain. The instantaneous distance between the point target and the SAR platform changes because the sensor on the platform advances along its path. In signal memory, the range variation, which is larger than the range resolution, leads to a migration through the range cells. This is called RCM. RCMC is the process which straightens out the curved target trajectory generated by RCM. Azimuth compression is then performed to synthesize the trajectory parallel to the Doppler axis into one pixel of an SAR image.

III. Proposed Signal Processing Algorithm for FMCW PolSAR Using Triangular LFM

In this section, we describe our FMCW PolSAR system using triangular LFM, and how it works. We propose a new signal processing algorithm suitable for our FMCW PolSAR system and discuss its advantages.

A. FMCW PolSAR System Using Triangular LFM

We designed an FMCW PolSAR system which is capable of radiating triangular LFM signals, as shown in Fig. 6. Specifications of the system are presented in Table II. Our system is composed of an LFM signal generator, double Ku-band upconverters, double Ku-band downconverters, and double baseband RXs. We coherently operate the system by fully synchronizing with a reference clock. Triangular LFM chirp signals with high linearity are generated by a direct digital synthesizer (DDS) to prevent spurious elements of beat frequency from being generated, which can cause target range ambiguity. The radio frequency (RF) switch in the system splits the LFM signals into upslope and downslope parts of the triangular LFM using a square wave. After upconverting the signals to Ku-band, the upconverter radiates the upslope parts of the signals as vertically polarized (V-pol) waves through a corrugated horn antenna with a power of about 39 dBm, while the other TX antenna radiates the downslope parts as horizontally polarized (H-pol) waves.

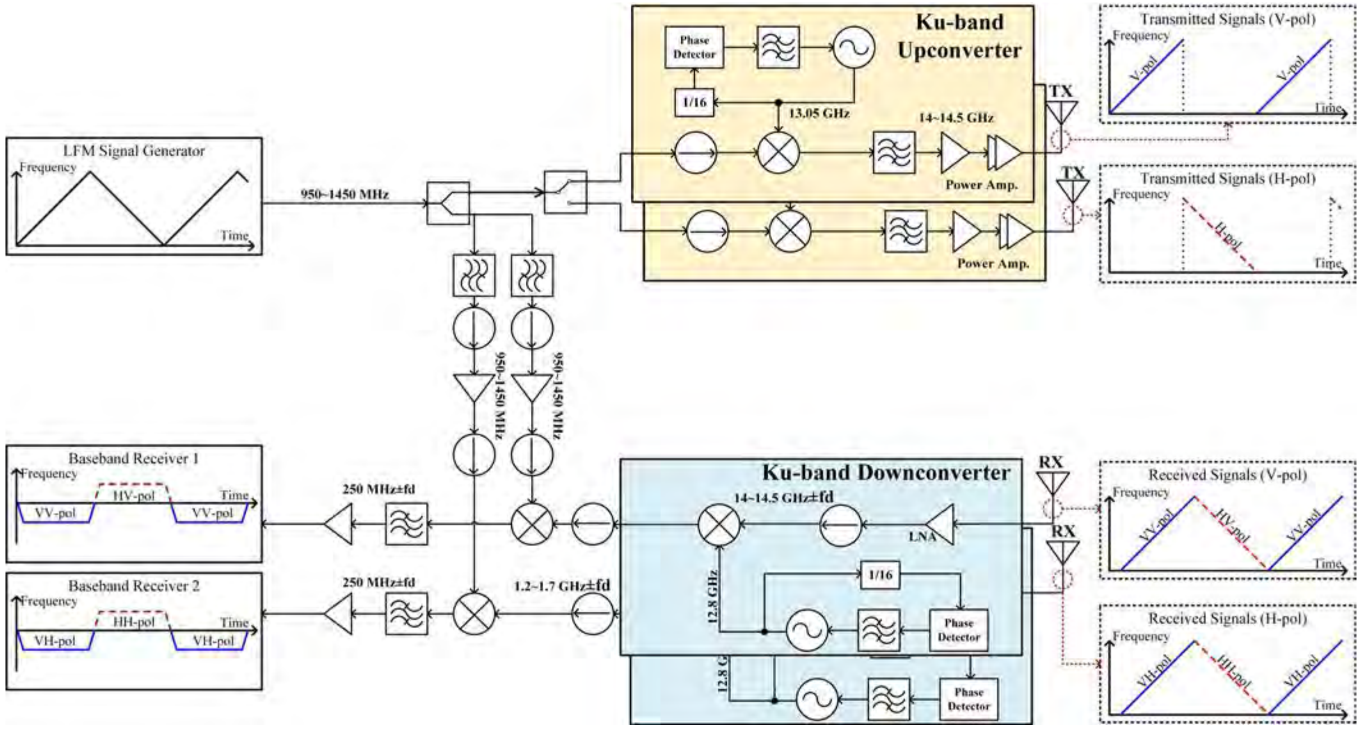

Fig. 6. Block diagram of the Ku-band automobile FMCW PolSAR system radiating the triangular LFM transmission signals. This figure briefly shows how two baseband RXs acquire four different single-polarization raw data.

TABLE II
SPECIFICATIONS OF THE KU-BAND AUTOMOBILE FMCW POLSAR SYSTEM

Parameters	Specifications
LFM Sweep Bandwidth	500 MHz
PRI	400 μs
LFM Sweep Type	Triangular LFM
Center Frequency	14.25 GHz
Transmission Power	39 dBm
Antenna Type	Corrugated Horn Antenna
Antenna Gain	21 dBi
Antenna 3dB Beamwidth	14.6°
Velocity of The Van	80 km/h
Look Angle	5 degree
Theoretical Range Resolution	30 cm
Theoretical Azimuth Resolution	12 cm
Sampling Rate	15 MS/s

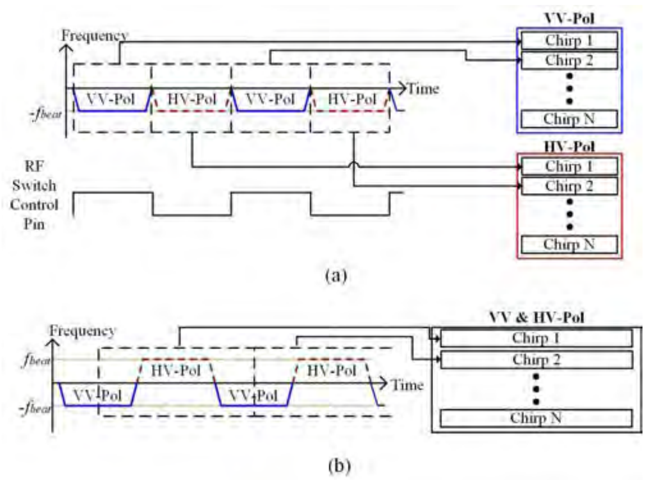

Fig. 7. How a raw data set is formed in the case of the sawtooth and triangular LFM transmission signals. (a) Two raw data sets are generated after accurately dividing into the VV-pol and HV-pol data by the square wave in the case of the sawtooth LFM. (b) Data set is generated after cutting data of a chirp corresponding to PRI without the square wave in the case of the triangular LFM.

The corrugated horn antenna offers the benefits of a wider bandwidth and lower sidelobes. After going through the V-pol RX antenna, the downconverter receives VV polarimetric (VV-pol) and HV polarimetric (HV-pol) signals, while the other downconverter receives VH polarimetric (VH-pol) and HH polarimetric (HH-pol) signals, after going through the H-pol RX antenna. VV and HV data are passed into the baseband RX after mixing the RF signal with the local oscillator signal, while VH and HH data are passed into the other baseband RX.

We extracted the digital quadrature demodulation data from the received signal in the baseband RXs.

Let us explain the benefit of using triangular LFM to configure the FMCW PolSAR hardware. Fig. 7 shows how raw data sets can be constructed in the baseband RXs when the radar radiates signals in the sawtooth and triangular LFM waveforms. Here, our explanation is limited to the VV-pol and HV-pol signals, using Fig. 7. The operation of the other polarimetric signals can be explained in the same way by replacing VV and HV with VH and HH, respectively.

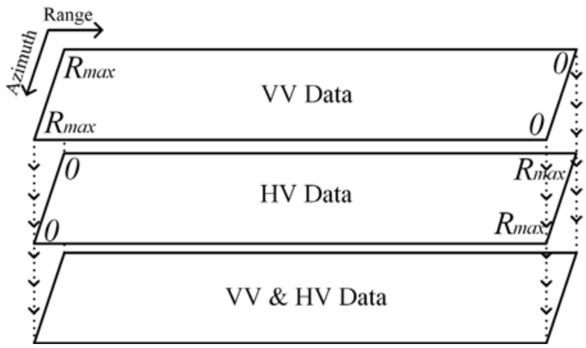

Fig. 8. Raw data set with symmetrical overlap between the VV and HV raw data. The other raw data set can be explained in the same way by replacing VV and HV with VH and HH, respectively.

The sawtooth LFM is commonly used as a transmit signal modulation in pulsed chirp radars, as well as in FMCW radar systems. When we utilize the sawtooth LFM, there is no way to separate the received data into two kinds of polarimetric raw data without a synchronization signal. Therefore, the received data must be divided into VV-pol and HV-pol raw data using the synchronization signal and then stored in the baseband RX. It is mandatory to separate each polarimetric data from the other polarimetric data at a certain timing using the synchronization signal.

In our system, we can exploit the square wave input to the RF switch control pin, which is used to accurately divide the received data into VV-pol and HV-pol data, as shown in Fig. 7(a). The separated chirps are stacked in each raw data set to form the VV-pol and HV-pol raw data sets. For this reason, for the sawtooth LFM, we must add an ADC for the synchronization signal to the digital data acquisition part of the baseband RX to configure the raw data set.

However, in the case of the triangular LFM, it is not essential to accurately cut the received data for each polarization using the square wave, because we separated the raw data set into two kinds of single-polarization raw data sets with our proposed algorithm. When using the triangular LFM, we cut out the received data corresponding to PRI, and then construct a raw data set regardless of the exact timing of the square wave. As a result, it is not necessary to add an ADC for the square wave to our system. This leads to simplification of the hardware configuration. In addition, VV and HV single-polarization images are generated using only one data set, whereas two data sets must be used for two kinds of single-polarization images in the case of the sawtooth LFM. Fig. 8 illustrates that the VV-pol and HV-pol raw data are symmetrically overlapped in the range Doppler domain based on the basic theory, which is mentioned in Section II.

In Section III-B, let us explain how our proposed algorithm processing is used to form VV-pol and HV-pol images from only one raw data set.

B. Proposed FMCW PolSAR Algorithm Based on RDA

An FMCW PolSAR system differs from pulsed PolSAR systems in that long sweep duration is used as a transmitted signal. The continuous motion on the radar platform within the sweep, which results in blurred SAR images, should be considered. Thus, when satellites or airplanes are equipped with FMCW PolSAR systems, a modified signal processing algorithm needs to be employed to compensate the movement while transmitting and receiving the signal without the conventional stop-and-go approximation [20].

In our case, we exploited an automobile as the radar platform, and its velocity was vastly lower than the commonly used platforms. We provided sweep signals for a short period using the DDS, and due to the slow platform velocity, an additional algorithm modification step was not needed to form a clear image.

Let us explain using our proposed algorithm for FMCW PolSAR to form a high-resolution color-coded image. We propose the algorithm shown in Fig. 9, based on the simple RDA mentioned in Section II. It is unessential to add a calibration step for the automobile FMCW PolSAR [5]. Let us assume that there is a point target on a targeted scene. We first perform range FFT and azimuth FFT steps on the raw data set containing VV-pol and HV-pol information. Since this is the single raw data set for two types of polarimetric images, the steps of the algorithm before dividing two kinds of polarimetric data have the effect of being applied to two kinds of polarimetric data simultaneously; this enables the total elapsed time of our algorithm to be reduced. After those steps, the trajectories of the single point target appear as two symmetrical parabolas. The solid line is the target trajectory in the VV-pol data and the dashed line is the target trajectory in the HV-pol data. We carry out a range inversion step to form a VV-pol image. This step reverses the raw data image in the range direction. Without the range inversion step, the VV-pol and HV-pol images appear symmetrically inverted. After generating four polarization images, it is essential to additionally work to align and match each image at the step to obtain an FMCW PolSAR image. That is why we add the range inversion step within the proposed algorithm. From (6), the raw data after the range inversion can be expressed as [19]

$$\begin{aligned} S_{rc}(f_\tau, f_\eta) &\approx A_0\, W_{\mathrm{a}}(f_\eta - f_{\eta_{\mathrm{c}}}) \\ &\quad \times \{W_{\mathrm{r,up}}[f_\tau - f_{\mathrm{beat,up}}] + W_{\mathrm{r,down}}[-f_\tau - f_{\mathrm{beat,down}}]\} \\ &\quad \times \exp\left\{-j\frac{4\pi f_{\mathrm{c}} R_0}{c}\right\} \exp\left\{-j\pi \frac{f_\eta^2}{K_{\mathrm{a}}}\right\}. \end{aligned} \tag{7}$$

From (5) and (7), the beat frequency of the RCM on the range envelope for the upslope part and downslope part of the triangular LFM can be derived as

$$f_{\mathrm{beat,up}} = f_{R_0} + f_{\mathrm{RCM}} \approx \frac{2\alpha R_0}{c} + \frac{\alpha R_0 \lambda^2 f_\eta^2}{4cV_{\mathrm{auto}}^2} \tag{8}$$

$$f_{\mathrm{beat,down}} = -f_{R_0} - f_{\mathrm{RCM}} \approx -\frac{2\alpha R_0}{c} - \frac{\alpha R_0 \lambda^2 f_\eta^2}{4cV_{\mathrm{auto}}^2} \tag{9}$$

where f_{R_0} is the beat frequency of the closest approach to the point target and f_{RCM} is the amount of RCM to correct. We can check to confirm whether the signs of the RCM of each polarimetric raw data are opposite.

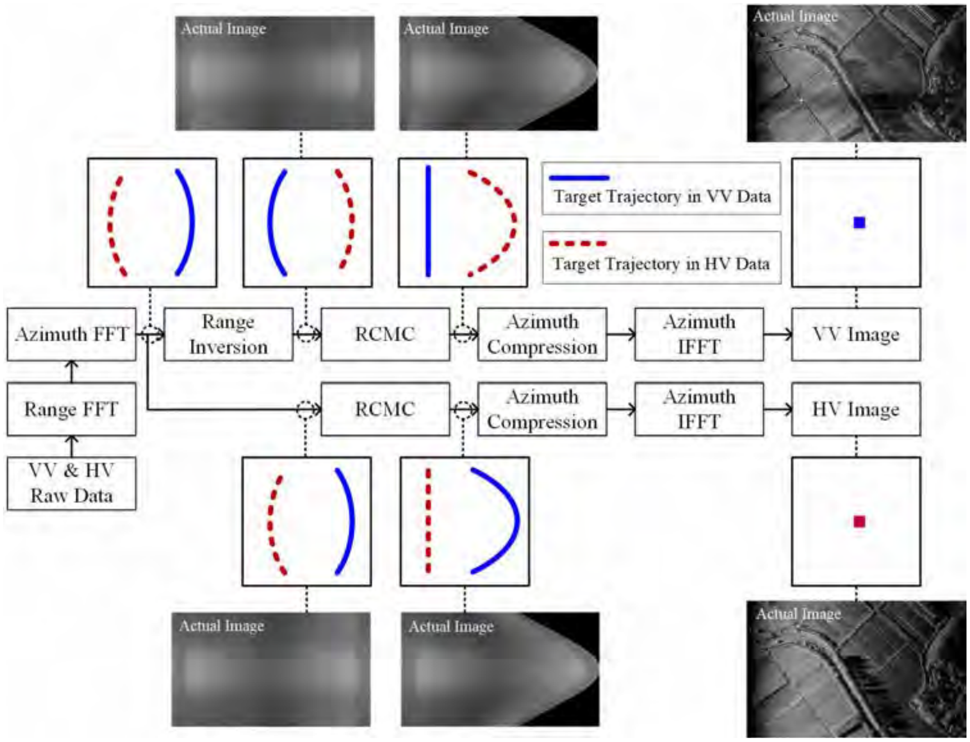

Fig. 9. Proposed FMCW PolSAR algorithm based on RDA. VV and HV single-polarization images are generated from the raw data set using the proposed algorithm. How to form the other single-polarization images can be explained in the same way by replacing VV and HV with VH and HH, respectively.

Conducting the RCMC step straightens out the target trajectory in the VV-pol data, while the target trajectory in the HV-pol data is more bent. We used a matched filter in the azimuth compression step to synthesize a target trajectory as a point pixel in a single-polarization SAR image. The target trajectory after the RCMC must be straight. For this reason, the straight target trajectory of the VV-pol data is synthesized into a point after the azimuth compression step and the azimuth IFFT, while the bent target trajectory of the HV-pol data is filtered out after the steps.

We then process the raw data set to form an HV-pol image using the same steps, except for the range inversion step, which is almost the same as the basic RDA. In this way, we are able to show that our proposed algorithm separates two kinds of polarimetric raw data in one data set, to form two different SAR images.

The other method for the VH-pol and HH-pol SAR images can be explained in the same way, by replacing VV and HV with VH and HH, respectively. As a result, using our proposed method, we can obtain all four types of single-polarization images for an FMCW PolSAR image from the two raw data sets.

In contrast, when using the sawtooth LFM, we repeated the basic RDA four times using four different raw data sets, and then produced four images. This confirms that our method can simplify the signal processing framework and reduce the elapsed time.

IV. Real Data Demonstration

A. Ku-Band Automobile FMCW Fully PolSAR Field Test

To validate our proposed algorithm, we carried out a Ku-band automobile FMCW PolSAR experiment using a van to collect raw data [5]. We set up a frame structure to hold four corrugated horn antennas, which were perfectly aligned toward the targeted scene, on the roof of the vehicle, as shown in Fig. 10. Two antennas were configured to radiate V-pol and H-pol waves and the other antennas were configured to receive V-pol and H-pol waves. Except for the parts fixed on the roof, the rest of our FMCW PolSAR system was mounted inside the vehicle.

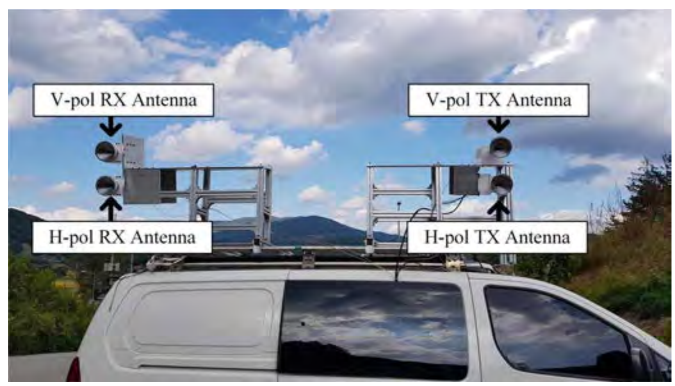

Fig. 10. TX and RX antenna configuration for radiating and receiving different polarimetric waves on a van.

We collected raw data in strip map mode on a highway in Gong-Ju, Korea. The highway rose to a height of about 100 m. The field test on the highway produced a swath range of about 600 m in the range direction. We simultaneously stored *IQ* raw data in the baseband RXs in the moving van, which traveled on the highway at a constant speed of 80 km/h. Fig. 11 shows an aerial photograph of the experiment site captured by a drone.

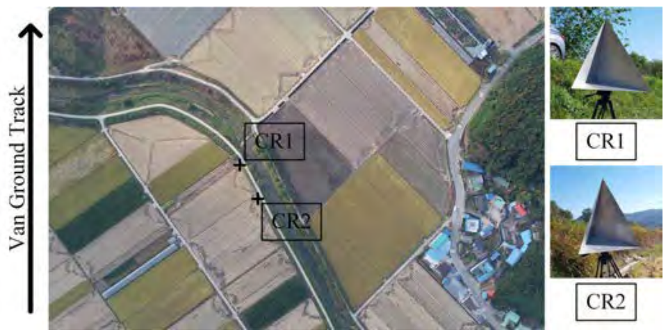

Fig. 11. Aerial photograph of Ku-band automobile FMCW PolSAR field test site. Two trihedral CRs were fixed near to the center of the test site for the CR profile analysis and the polarimetric calibration.

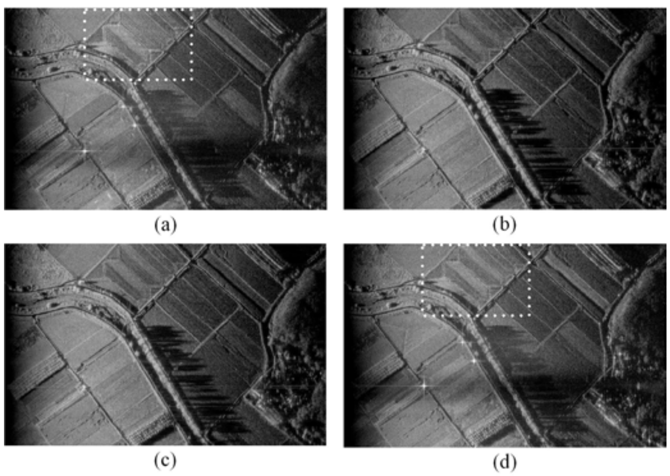

Fig. 12. Single look complex images of the experiment site with FMCW PolSAR system using the triangular LFM. The images were processed using our proposed algorithm. (a) HH-pol image. (b) HV-pol image. (c) VH-pol image. (d) VV-pol image.

We deployed two trihedral corner reflectors (CRs) near the center of the targeted scene for CR profile analysis. Then, we utilized the CRs not only as calibration targets but also to assess calibration performance.

B. Ku-Band Automobile FMCW Fully PolSAR Image

From the experiment on the highway, we obtained two raw data sets for processing into a single look complex image of each polarized channel. We then processed the raw data sets to form four polarized channel images using our proposed algorithm, which was employed to process the raw data set into two different polarization images. We provided HH-pol, HV-pol, VH-pol, and VV-pol images of the experiment site, as shown in Fig. 12. The HH-pol and VH-pol images were produced using the proposed algorithm from the raw data set stored in the H-pol baseband RX, as shown in Fig. 12(a) and (c), respectively, while the HV-pol and VV-pol images were produced from the other raw data set stored in the V-pol baseband RX, as shown in Fig. 12(b) and (d), respectively. It is obvious that two kinds of single-polarization images were formed from the single data set using the proposed algorithm. Hence, this result is clear evidence that the proposed algorithm is valid for the FMCW PolSAR system using the triangular LFM.

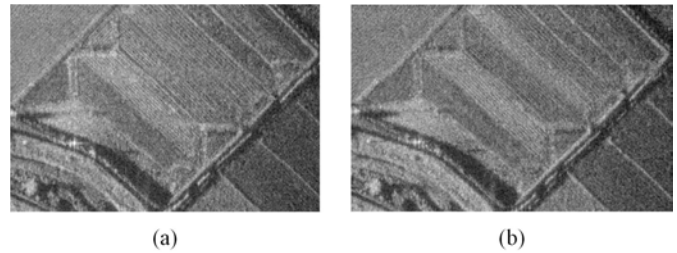

Fig. 13. Enlarged images in the dotted square of Fig. 12(a) and (d). (a) HH-pol image. (b) VV-pol image.

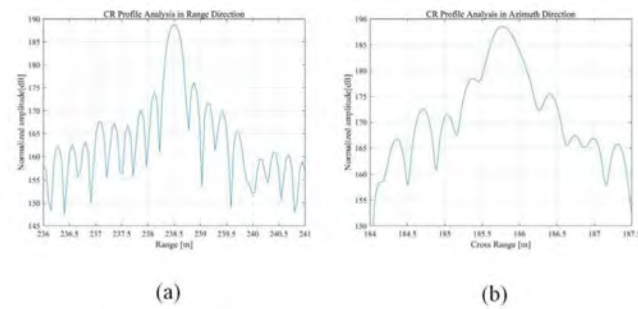

Fig. 14. Results of the CR analysis in the VV-pol image with CR 1 shown in Fig. 11. (a) Range profile of CR 1. (b) Cross-range profile of CR 1.

TABLE III
RESULTS OF THE CR ANALYSIS IN THE VV-POL IMAGE WITH CR 1

Parameters	Range Direction	Azimuth Direction
Peak level	187.15 dB	187.15 dB
PSLR	-10.37 dB	-9.02 dB
Resolution at -3dB	24.87 cm	32.41 cm

TABLE IV
COMPUTATION TIME FOR SIGNAL PROCESSING WITH THE PROPOSED ALGORITHM

Parameters	Basic RDA $\times$ 4	Our Algorithm
Computation time	489.6 sec	353.2 sec

Fig. 13 presents enlarged images in the dotted square of HH-pol and VV-pol images, as shown in Fig. 12(a) and (d). We experimented with our PolSAR system at harvest time. After harvest, the remaining crops lay on the ground in a specific direction. Fig. 13 shows that the two images are different because crops have different polarization reflection features depending on the direction in which they lie, even though HH-pol and VV-pol are co-polarization states. Fig. 14 and Table III describe results of CR analysis in the VV-pol image with CR 1 shown in Fig. 11. Peak sidelobe ratio (PSLR) is the ratio of the peak level of the largest sidelobe and that of the main lobe. These results indicate that our proposed FMCW PolSAR system is capable of providing high-resolution PolSAR images.

Table IV shows the computation time for a PolSAR image in the experiment to compare the signal processing efficiencies

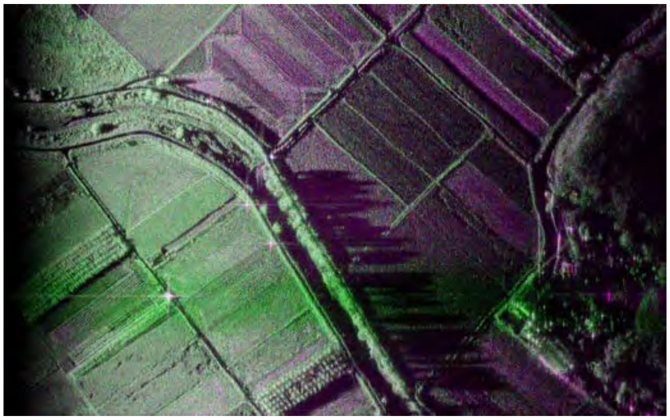

Fig. 15. Calibrated Ku-band automobile FMCW fully PolSAR image of Gong-Ju, South Korea, rendered in the Pauli RGB basis, where red is [HH − VV], green is [HV], and blue is [HH + VV]. The image covers an area of 310 m (azimuth direction) × 630 m (range direction). This image indicates that our proposed algorithm is appropriate for an FMCW PolSAR system using triangular LFM.

of basic RDA and our proposed algorithm. We repeated the basic RDA four times and measured the computation time as a control. Table IV shows that the computation time obtained with our proposed algorithm is shorter than that obtained with basic RDA; this means that our signal processing technique for FMCW PolSAR is efficient compared with simply conducting the basic RDA.

Using a 2 × 2 complex scattering matrix, the basic concept of PolSAR can be expressed as [21]–[23]

$$\begin{bmatrix} E_{\mathrm{H}}^{\mathrm{r}} \\ E_{\mathrm{V}}^{\mathrm{r}} \end{bmatrix} = \frac{\exp(-jkr)}{r} \cdot \begin{bmatrix} S_{\mathrm{HH}} & S_{\mathrm{HV}} \\ S_{\mathrm{VH}} & S_{\mathrm{VV}} \end{bmatrix} \begin{bmatrix} E_{\mathrm{H}}^{\mathrm{t}} \\ E_{\mathrm{V}}^{\mathrm{t}} \end{bmatrix} \tag{10}$$

where $\vec{E}^{\mathrm{t}}$ is the 2-D transmitted plane wave vector, $\vec{E}^{\mathrm{r}}$ is the 2-D received plane wave vector, $[S]$ is complex scattering matrix containing the four complex scattering amplitudes, k is the wavenumber, and $\exp(-jkr)/r$ indicates the attenuation and the phase shift generated by the distance between targets and the PolSAR sensor, respectively. We conducted the calibration step for FMCW PolSAR using a trihedral CR to obtain accurate polarimetric information [7]. The expected scattering matrix of the trihedral CR can be expressed as [24], [25]

$$[S]_{\mathrm{trihedral}} = \begin{bmatrix} S_{\mathrm{HH}} & S_{\mathrm{HV}} \\ S_{\mathrm{VH}} & S_{\mathrm{VV}} \end{bmatrix} = \begin{bmatrix} 1 & 0 \\ 0 & 1 \end{bmatrix}. \tag{11}$$

After calibration, we produced a Ku-band automobile FMCW fully PolSAR image, as shown in Fig. 15, rendered using a Pauli decomposition basis. The image covers an area of 310 m × 630 m. We confirmed that Fig. 15 shows more information than the single-polarization SAR images presented in Fig. 10. This result indicates that our proposed algorithm based on RDA is appropriate for an FMCW PolSAR system using triangular LFM, and FMCW PolSAR image processing.

V. Conclusion

In summary, this article introduces a new signal processing method for an FMCW fully PolSAR system transmitting triangular LFM continuous waves. We described different FMCW SAR signal models for the sawtooth and triangular waveform LFM types, based on the theoretical background presented in Section II. This indicated that two kinds of single-polarization raw data sets were symmetrically overlapped on a raw data set in the range Doppler domain when the FMCW SAR sensor radiated triangular LFM waves.

We prepared and tested a Ku-band automobile FMCW fully PolSAR system using the triangular LFM, and explained how it worked. A proposed algorithm based on RDA was developed to form two kinds of single-polarization images from one raw data set. With the algorithm, our FMCW PolSAR system provides both a simplified hardware configuration and effective PolSAR image processing. The performance of the proposed system and algorithm was verified with experiment results.

This work enables a new direction in SAR polarimetry in FMCW radar systems. The method developed for an automobile FMCW fully PolSAR system using triangular LFM is not more challenging than using sawtooth LFM and, in certain aspects, is more straightforward.

The proposed system requires much further validation; however, considerable study has been expended on a real data demonstration to realize that potential. Similar attention has been paid to the design of both the FMCW PolSAR system and the algorithm. Further research should focus on improving several techniques in SAR polarimetry, e.g., calibration [26], [27], speckle filtering [28], classification [29], and scattering model configuration [30], [31], to realize an operational FMCW PolSAR system using triangular LFM.

References

[1] D.-H. Shin, D.-H. Jung, D.-C. Kim, J.-W. Ham, and S.-O. Park, "A distributed FMCW radar system based on fiber-optic links for small drone detection," *IEEE Trans. Instrum. Meas.*, vol. 66, no. 2, pp. 340–347, Feb. 2017.

[2] C. Q. Mayoral *et al.*, "Water content continuous monitoring of grapevine xylem tissue using a portable low-power cost-effective FMCW radar," *IEEE Trans. Geosci. Remote Sens.*, vol. 57, no. 8, pp. 5595–5605, Aug. 2019.

[3] C. Will, P. Vaishnav, A. Chakraborty, and A. Santra, "Human target detection, tracking, and classification using 24-GHz FMCW radar," *IEEE Sensors J.*, vol. 19, no. 17, pp. 7283–7299, Sep. 2019.

[4] A. Meta, P. Hoogeboom, and L. P. Ligthart, "Signal processing for FMCW SAR," *IEEE Trans. Geosci. Remote Sens.*, vol. 45, no. 11, pp. 3519–3532, Nov. 2007.

[5] D.-H. Jung, H.-S. Kang, C.-K. Kim, J. Park, and S.-O. Park, "Sparse scene recovery for high-resolution automobile FMCW SAR via scaled compressed sensing," *IEEE Trans. Geosci. Remote Sens.*, vol. 57, no. 12, pp. 10136–10146, Dec. 2019.

[6] R. Wang, O. Loffeld, H. Nies, S. Knedlik, M. Hägelen, and H. Essen, "Focus FMCW SAR data using the wave number domain algorithm," *IEEE Trans. Geosci. Remote Sens.*, vol. 48, no. 4, pp. 2109–2118, Apr. 2010.

[7] A. Liu, F. Wang, H. Xu, and L. Li, "N-SAR: A new multichannel multimode polarimetric airborne SAR," *IEEE J. Sel. Topics Appl. Earth Observ. Remote Sens.*, vol. 11, no. 9, pp. 3155–3166, Sep. 2018.

[8] G. E. Gunn, C. R. Duguay, D. K. Atwood, J. King, and P. Toose, "Observing scattering mechanisms of bubbled freshwater lake ice using polarimetric RADARSAT-2 (C-band) and UW-scat (X- and ku-bands)," *IEEE Trans. Geosci. Remote Sens.*, vol. 56, no. 5, pp. 2887–2903, May 2018.

[9] B. Zhang *et al.*, "Ocean vector winds retrieval from C-band fully polarimetric SAR measurements," *IEEE Trans. Geosci. Remote Sens.*, vol. 50, no. 11, pp. 4252–4261, Nov. 2012.

[10] Y. Yamaguchi and T. Moriyama, "Polarimetric detection of objects buried in snowpack by a synthetic aperture FM-CW radar," *IEEE Trans. Geosci. Remote Sens.*, vol. 34, no. 1, pp. 45–51, Jan. 1996.

[11] S. Navneet, A. Roy, and C. Bhattacharya, "High-resolution SAR image generation by subaperture processing of FMCW radar signal," *IEEE Geosci. Remote Sens. Lett.*, vol. 11, no. 11, pp. 1866–1870, Nov. 2014.

[12] W.-Q. Wang, Q. Peng, and J. Cai, "Waveform-diversity-based millimeter-wave UAV SAR remote sensing," *IEEE Trans. Geosci. Remote Sens.*, vol. 47, no. 3, pp. 670–691, Mar. 2009.

[13] A. Meta and P. Hoogeboom, "Signal processing algorithms for FMCW moving target indicator synthetic aperture radar," in *Proc. IEEE Int. Geosci. Remote Sens. Symp.*, Seoul, South Korea, Jul. 2013, pp. 316–319.

[14] B.-L. Cho, Y.-K. Kong, H.-G. Park, and Y.-S. Kim, "Automobile-based SAR/InSAR system for ground experiments," *IEEE Geosci. Remote Sens. Lett.*, vol. 3, no. 3, pp. 401–405, Jul. 2006.

[15] R. Wang, Y.-H. Luo, Y.-K. Deng, Z.-M. Zhang, and Y. Liu, "Motion compensation for high-resolution automobile FMCW SAR," *IEEE Geosci. Remote Sens. Lett.*, vol. 10, no. 5, pp. 1157–1161, Sep. 2013.

[16] H.-C. Lee, E. S. Kang, S. B. Ryu, S.-G. Lee, S. S. Yong, and C. H. Jung, "Stripmap mode test of X-band AutoSAR prototype using measurement instruments," in *Proc. IEEE Int. Geosci. Remote Sens. Symp. (IGARSS)*, Milan, Italy, Jul. 2015, pp. 1789–1792.

[17] M.-T. Dao, D.-H. Shin, Y.-T. Im, and S.-O. Park, "A two sweeping VCO source for heterodyne FMCW radar," *IEEE Trans. Instrum. Meas.*, vol. 62, no. 1, pp. 230–239, Jan. 2013.

[18] J. Park, S. Park, D.-H. Kim, and S.-O. Park, "Leakage mitigation in heterodyne FMCW radar for small drone detection with stationary point concentration technique," *IEEE Trans. Microw. Theory Techn.*, vol. 67, no. 3, pp. 1221–1232, Mar. 2019.

[19] I. G. Cumming, and F. H. Wong, *Digital Processing of Synthetic Aperture Radar Data: Algorithms and Implementation*. Norwood, MA, USA: Artech House, 2005.

[20] A. Ribalta, "Time-domain reconstruction algorithms for FMCW-SAR," *IEEE Geosci. Remote Sens. Lett.*, vol. 8, no. 3, pp. 396–400, May 2011.

[21] A. Moreira, P. Prats-Iraola, M. Younis, G. Krieger, I. Hajnsek, and K. P. Papathanassiou, "A tutorial on synthetic aperture radar," *IEEE Geosci. Remote Sens. Mag.*, vol. 1, no. 1, pp. 6–43, Mar. 2013.

[22] G. Sinclair, "The transmission and reception of elliptically polarized waves," *Proc. IRE*, vol. 38, no. 2, pp. 148–151, Feb. 1950.

[23] J.-S. Lee and E. Pottier, *Polarimetric Radar Imaging: From Basics to Applications*. Boca Raton, FL, USA: CRC Press, 2009.

[24] R. Touzi and M. Shimada, "Polarimetric PALSAR calibration," *IEEE Trans. Geosci. Remote Sens.*, vol. 47, no. 12, pp. 3951–3959, Dec. 2009.

[25] A. Freeman, "SAR calibration: An overview," *IEEE Trans. Geosci. Remote Sens.*, vol. 30, no. 6, pp. 1107–1121, Nov. 1992.

[26] T. L. Ainsworth, L. Ferro-Famil, and J.-S. Lee, "Orientation angle preserving a posteriori polarimetric SAR calibration," *IEEE Trans. Geosci. Remote Sens.*, vol. 44, no. 4, pp. 994–1003, Apr. 2006.

[27] S. Baffelli, O. Frey, C. Werner, and I. Hajnsek, "Polarimetric calibration of the Ku-band advanced polarimetric radar interferometer," *IEEE Trans. Geosci. Remote Sens.*, vol. 56, no. 4, pp. 2295–2311, Apr. 2018.

[28] J.-S. Lee, M. R. Grunes, and G. de Grandi, "Polarimetric SAR speckle filtering and its implication for classification," *IEEE Trans. Geosci. Remote Sens.*, vol. 37, no. 5, pp. 2363–2373, Sep. 1999.

[29] J.-S. Lee, M. R. Grunes, T. L. Ainsworth, L.-J. Du, D. L. Schuler, and S. R. Cloude, "Unsupervised classification using polarimetric decomposition and the complex wishart classifier," *IEEE Trans. Geosci. Remote Sens.*, vol. 37, no. 5, pp. 2249–2258, Sep. 1999.

[30] A. Freeman and S. L. Durden, "A three-component scattering model for polarimetric SAR data," *IEEE Trans. Geosci. Remote Sens.*, vol. 36, no. 3, pp. 963–973, May 1998.

[31] Y. Yamaguchi, T. Moriyama, M. Ishido, and H. Yamada, "Four-component scattering model for polarimetric SAR image decomposition," *IEEE Trans. Geosci. Remote Sens.*, vol. 43, no. 8, pp. 1699–1706, Aug. 2005.

Dae-Hwan Jung was born in Seoul, South Korea, in 1988. He received the B.S. degree in electronic and electrical engineering from Sungkyunkwan University, Suwon, South Korea, in 2014, and the M.S. degree in electrical engineering from the Korea Advanced Institute of Science and Technology, Daejeon, South Korea, in 2016, where he is currently pursuing the Ph.D. degree.

His current research interests include the design of frequency modulation continuous wave (FMCW) radar systems, FMCW synthetic aperture radar (SAR), and SAR signal processing.

Do-Hoon Kim received the B.S. degree in electrical engineering from Yonsei University, Seoul, South Korea, in 2017. He is currently pursuing the M.S. degree in electrical engineering with the Korea Advanced Institute of Science and Technology, Daejeon, South Korea.

His current research interest is radar signal processing.

Muhammad Tayyab Azim was born in Pakistan, in 1987. He received the B.E. degree in avionics engineering from the National University of Sciences and Technology (NUST), Islamabad, Pakistan, in 2009, and the M.S. degree in electrical engineering from the University of Surrey, Guildford, U.K., in 2011. He is currently pursuing the Ph.D. degree in electrical engineering with the Korea Advanced Institute of Science and Technology (KAIST), Daejeon, South Korea.

His research interests include electromagnetics, antenna design, and microwave components design.

Junhyeong Park (Member, IEEE) received the B.S. and M.S. degrees in electrical engineering from the Korea Advanced Institute of Science and Technology (KAIST), Daejeon, South Korea, in 2015 and 2017, respectively, where he is currently pursuing the Ph.D. degree in electrical engineering.

His current research interests include radar systems for defense, drone detection radar, radar imaging, target recognition/classification, and radar signal processing.

Seong-Ook Park (Senior Member, IEEE) was born in Yeongcheon, South Korea, in 1964. He received the B.S. degree in electrical engineering from Kyungpook National University, Daegu, South Korea, in 1987, the M.S. degree in electrical engineering from the Korea Advanced Institute of Science and Technology (KAIST), Daejeon, South Korea, in 1989, and the Ph.D. degree in electrical engineering from Arizona State University, Tempe, AZ, USA, in 1997.

From 1989 to 1993, he was a Research Engineer with Korea Telecom, Daejeon, where he was involved in microwave systems and networks. He was with the Telecommunication Research Center, Arizona State University, until 1997. Since 1997, he has been a Professor with KAIST. His current research interests include antenna, radar system, and analytical and numerical techniques in the area of electromagnetics.

Dr. Park is a member of Pi Kappa Phi.